The Tumor Immune Microenvironment Drives a Prognostic Relevance That Correlates with Bladder Cancer Subtypes

Carolin Pfannstiel[1]; Pamela L. Strissel[2]; on behalf of the BRIDGE Consortium, Germany, Katherine B. Chiappinelli[3]; Danijel Sikic[4], Sven Wach[4], Ralph M. Wirtz[5]; on behalf of the BRIDGE Consortium, Germany, Adrian Wullweber[1]; Helge Taubert[4], Johannes Breyer[6], Wolfgang Otto[6], Thomas Worst[7], Maximilian Burger[6], Bernd Wullich[5], Christian Bolenz[8]; on behalf of the BRIDGE Consortium, Germany, Nicole Fuhrich[1], Carol I. Geppert[1]; Veronika Weyerer[1], Robert Stoehr[1], Simone Bertz[1], Bastian Keck[4], Franziska Erlmeier[9], Philipp Erben[7], Arndt Hartmann[1], Reiner Strick[2], and Markus Eckstein[1]; on behalf of the BRIDGE Consortium, Germany

Abstract

Muscle-invasive bladder cancer (MIBC) represents approximately two-thirds of invasive urothelial bladder cancers (UBC) and has high morbidity and mortality. Men are over 3-fold more frequently affected by UBC than women. Despite intensive efforts to improve patient treatment and outcome, two-thirds of patients with UBC will have a recurrence or disease progression within 5 years. We demonstrated that the quantity and spatial distribution of stromal tumor-infiltrating lymphocytes (sTIL) within the tumor immune microenvironment (TIME) predict stages of tumor inflammation, subtypes, and patient survival and correlate with expression of immune checkpoints in an analysis of 542 patients with MIBC. High sTILs indicated an inflamed subtype with an 80% 5-year DSS, and a lack of immune infiltrates identified an uninflamed subtype with a survival rate of less than 25%. A separate immune evading phenotype with upregulated immune checkpoints associated with poor survival. Within the TIME are tertiary lymphoid structures (TLS), which can mediate antitumor activity via immune cells. High TLS amounts and close tumor distance correlated significantly with an inflamed phenotype and favorable survival. The uninflamed and evasion phenotypes showed lowest TLS numbers, farthest tumor distances, and shortest survival. High inflammation also correlated with increased neoantigen load and mutational burden. Patients treated with adjuvant chemotherapy showed a favorable prognosis, which was dependent on high sTILs. Determination of sTILs and tumor subtypes may stratify therapy success and patient survival, and considering sTILs can easily be quantified using simple morphologic parameters, like hematoxylin and eosin, sTILs can be implemented for predicting patient survival in a routine manner.

Introduction

Urothelial bladder cancer (UBC) is one of the 10th most common malignancies worldwide and the second most common cancer of the genitourinary tract (1). Current therapy for muscle-invasive bladder cancer (MIBC) consists of radical cystectomy, with bilateral lymphadenectomy in combination with platinum-based perioperative chemotherapy, in patients with extravesical tumors and/or lymph node metastasis (2). MIBC is characterized by a poor 5-year survival of 40%–60% (2).

Molecular characterization of MIBC demonstrates two major phenotypes, luminal and basal tumors with significant prognostic and predictive value (3, 4). Immunotherapeutic agents offer new therapy options for patients with metastasized UBC (5). The FDA has approved immunotherapeutic agents targeting PD-1 or

PD-L1, which have demonstrated prolonged stable responses in metastatic UBC (6). Therapeutic response of many tumors, including UBC, correlates with amounts of tumor-infiltrating lymphocytes (TIL), tertiary lymphoid structures (TLS), the number of neoantigens, and tumor mutational burden (TMB; refs. 5, 7–9).

TILs in the tumor immune microenvironment (TIME) have been researched for over 40 years, with one initial article describing infiltrating T cells in UBC (10). TILs can consist of T, B, and natural killer (NK) cells. CD8$^+$ cytotoxic T-effector cells (T$_{EFF}$) play a critical role in restraining tumor development, whereas CD4$^+$ Th cells can have pro- or antitumor effects (11). TILs predict a better prognosis for patients with different tumor types, including colorectal, breast, and ovarian cancers (12–15). Immune gene expression patterns are enriched in UBC and expression of immune checkpoint genes is enhanced in tumors, for example, T-cell inflammation–related genes (16, 17). Only limited data of small patient cohorts have indicated positive prognostic relevance of TILs for patient survival (18–20). Because the presence of TILs seems to predict response to immuno-oncologic treatments, characterization of the MIBC TIME is needed (5).

We present comprehensive data on the role of stromal tumor-infiltrating lymphocytes (sTIL) in MIBC. sTILs quantities predicted different immune phenotypes, survival, and tumor subtypes in 542 patients with MIBC. Five inflammation-associated genes correlated with sTILs and delineated high, low, or absent levels of tumor inflammation, which correlated with tumor subtypes and patient survival. Using IHC, we revealed detailed knowledge about spatial tumor organization and identified three different inflammatory phenotypes and a unique tumor evasion phenotype, all affecting patient outcomes. We further showed a significant correlation of sTILs with *APOBEC* mutational load, neoantigens, and TMB.

Materials and Methods

Study cohorts and histopathologic review

We investigated two independent MIBC cohorts: (i) the Comprehensive Cancer Center Erlangen Metropol Region Nuremberg cohort (CCC-EMN; $n = 135$); and (ii) The Cancer Genome Atlas bladder cancer cohort (TCGA BLCA) cohort ($n = 407$). Patients within both cohorts were treated with radical cystectomy and bilateral lymph node dissection. The CCC-EMN cohort initially consisted of 148 MIBC cases, of which 13 were excluded due to the following issues: 8 were metastasized and for 5 cases, no representative tissue was available. Out of the TCGA BLCA cohort ($n = 413$), 6 cases were excluded due to missing RNAseq data and DNA mutational analysis. No further exclusion criterions were applied.

For analysis in the CCC-EMN cohort, standard formalin-fixed paraffin-embedded (FFPE) tumor tissues (paraffin blocks) were collected from pathologic routine case files. The blocks were stored at room temperature until further use. For each analysis, fresh tissue cuts were taken from the blocks.

The CCC-EMN cohort was reevaluated and classified according to the most recent TNM classification (2017) and the WHO 2016 classification of genitourinary tumors. Clinical, pathologic, and molecular data of the TCGA cohort were updated accordingly (3). Clinicopathologic data are depicted in Supplementary Table S1.

sTILs assessment

sTILs were analyzed on hematoxylin and eosin (H&E)-stained tissue sections of both cohorts by two observers (M. Eckstein and C. Pfannstiel). TCGA images were accessed via the Cancer Digital Slide Archive (cancer.digitalslidearchive.net). sTILs were scored in the desmoplastic tumor stroma according to a validated methodology of the International Working Group on TILs (Supplementary Fig. S1A and S1B; refs. 13, 20). Large fibrotic and necrotic areas and sTILs within noninvasive papillary tumor regions were excluded (20). sTILs of normal healthy bladder tissues ($n = 65$) were also scored according to the above criteria (Supplementary Fig. S1A). The normal tissue samples were collected from healthy patients without the diagnosis of bladder cancer or inflammatory diseases of the bladder.

CCC-EMN: Tissue microarray

FFPE blocks with at least 50% tumor (minimal tumor size 5×5 mm), well delimited invasion borders, and without necrotic areas or granulomatous inflammation were selected from each patient out of the CCC-EMN cohort ($n = 148$). H&E-stained slides were scanned (Panoramic P250, 3DHistech) and annotated with CaseViewer 2.0 (3DHistech). Four cores (diameter 1 mm; two cores from the invasion front and two cores from the tumor center) were isolated using the TMA-Grandmaster (3DHistech; refs. 21, 22).

CCC-EMN: IHC and analysis of PD-L1 and TLSs

IHC was performed on 4-μm tissue sections on a Ventana BenchMark Ultra autostainer (Ventana) according to accredited staining protocols (https://www.dakks.de/en) using the following antibodies: PD-L1 (SP263 assay, Ventana), CD3 (F7.2.38, monoclonal mouse; Thermo Fisher Scientific; dilution 1:50), CD8 (C8/144B, mouse monoclonal; Thermo Fisher Scientific; dilution 1:50), CD79a (JCB117, mouse monoclonal; Zytomed Systems; dilution 1:50), PD-1 (NAT105, mouse monoclonal; Ventana), CD68 (PG-M1, mouse monoclonal; Thermo Fisher Scientific; dilution 1:60), and CD56 (MRQ-42, monoclonal mouse; Cell Marque; dilution 1:50; example pictures depicted in Supplementary Fig. S1C).

PD-L1$^+$ immune cells (IC) and tumor cells were scored on TMAs by two pathologists (A. Hartmann and M. Eckstein) according to the distributor's PD-L1 scoring algorithm (21, 22). Positivity of tumor cells was scored as a percentage with specific, membranous staining using the PD-L1 assay described above (Ventana SP263). Number of ICs was scored as the percentage ratio of the area occupied by positive ICs per tumor area (22). Data ranges based from the hierarchical cluster analysis for defining absence, very low, low, moderate, or high expression of these variables were as follows: (i) sTILs: very low = interquartile range (IQR) 1%–5%, low = IQR 5%–20%, moderate = IQR 10%–27.5%, and high = IQR 15%–75%; (ii) PD-1$^+$ ICs: IQR 0.81–3.16, low = IQR 2.0–4.57, moderate = IQR 3.85–5.1, and high = IQR 4.90–7.12; (iii) PD-L1$^+$ ICs: very low = IQR 0%–0.5%, low = IQR 0.-3.0%, high = IQR 7.0%–15.7%; (iv) PD-L1$^+$ TCs: absent = IQR 0%, moderate = IQR 0%–27.5%, high = IQR 53.8%–100%.

TLSs were scored on digitalized whole mount IHC sections stained with the abovementioned antibodies by two observers (M. Eckstein and C. Pfannstiel). Slides were scanned with a slide scanner (Panoramic P250, 3DHistech) and viewed with the CaseViewer 2.0 (3DHistech). Total amounts of TLSs were scored in the

tumor surrounding tissue and within the tumor tissue. TLSs were defined by the following criteria: (i) germinal centers with CD79a$^+$ B cells; (ii) CD68$^+$ macrophages; and (iii) CD3$^+$CD8$^+$ T$_{EFF}$ cells. The TLS minimal distance (in μm) was also measured with the CaseViewer 2.0 (3DHistech). TLS distance of TLSs with direct contact to the tumor mass at the invasive margin or with localization in the tumor was scored as 0 μm.

CCC-EMN: Automated image analysis by the Definiens Developer Software

For this analysis, TMA sections stained for CD3, CD8, PD-1, CD68, and CD56 were scanned with a slide scanner (Panoramic P250, 3DHistech). The files were imported into the Definiens Developer Software (Definiens AG). Tumor, normal, and stroma tissue and empty spaces on all TMA cores were segregated by a machine-learning approach (Composer module of Definiens Developer Software). Correct area detection was visually checked for all cores with the Definiens Tissue Studio (Definiens AG) "region of interest correction" and revised to include digitally undetected tumor cells and exclude staining artifacts (diaminobenzidine remnants) and empty spaces. CD3$^+$, CD8$^+$, PD-1$^+$, CD68$^+$, and CD56$^+$ immune cells (IC) were then quantified automatically by the software algorithm. Cell counts were obtained as counts per mm^2 and log$_2$-transformed for further analysis.

CCC-EMN: Molecular subtyping via NanoString

RNA was isolated from five 10-μm FFPE sections with at least 50% tumor of using the Maxwell Promega RNA purification Kit (Promega). Sections were deparaffinized with xylol and rehydrated with ethanol. Fractionated tumor tissue was digested with 30 μL Proteinase K (Promega), and RNA was extracted by an automated magnetic bead-based approach using the Promega Maxwell (Promega). Purified RNA was measured via a Qubit 4.0 Fluorometer (Thermo Fisher Scientific) according to NanoString assay recommendations. Four-hundred nanograms of RNA of each sample was hybridized with 8 μL of the NanoString detection probe–containing mastermix for 16 hours at 67°C on a Mastercycler X50p (Eppendorf AG). After hybridization, samples were loaded in standard 12-stripe NanoString tubes and purified by the nCounter Prep-station (NanoString). Purified samples were loaded in the analysis cartridge by the Prep-station, and the cartridge containing purified RNA hybrids was analyzed via the MaxFlex nCounter system (NanoString). According to NanoString recommendations, no technical replicates were analyzed. A sample of an MIBC patient was used as an external tissue control. For internal controls, every codeset library of NanoString contains premade positive and negative control. A custom NanoString panel of 21 genes for luminal and basal differentiation were selected according to MD Anderson Cancer Center (MDACC, Houston, TX) subtyping approach (ref. 23; Supplementary Table S2). Gene counts were normalized using two reference genes (SDHA, HPRT1) and log$_2$-transformed for further analysis by the nSolver 4.0 software (NanoString). Further analysis was carried out with JMP SAS 13.2 (SAS Institute).

CCC-EMN: qRT-PCR

RNA was extracted on the basis of a magnetic bead approach (RNA-Xtract-Kit, STARTIFYER) using a single 10-μm FFPE section with tumor content of at least 50% on a STRATIFYER XTRAKT platform (STRATIFYER, Molecular Pathology GmbH; ref. 21).

RNA/cDNA concentration was assessed via a Qubit 4.0 Fluorometer (Thermo Fisher Scientific). Expression of CD3Z (CD247), CD8A, PD-L1 (CD274), PD-1 (PDCD1), and CXCL9 were assessed in triplicates by qRT-PCR on a Versant kPCR system (Siemens) according to the following protocol using approved qRT-PCR-Kits from STRATIFYER Molecular Pathology (STRATIFYER; refs. 24, 25): 5 minutes at 50°C, 20 seconds at 95°C followed by 40 cycles of 15 seconds at 95°C and 60 seconds at 60°C. Forty amplification cycles were applied, and the cycle quantification threshold (C_q) values of target genes and the reference gene for each sample (S) were estimated as the median of triplicate measurements. Primers were purchased from Eurogentec. Primer sequences are depicted in Supplementary Table S2.

Data were normalized, using three reference genes (RPL37A, B2M, CALM2) according to MIQE guidelines (26). Final values were generated using ΔC_t from the total number of cycles to ensure that normalized gene expression obtained is proportional to the corresponding mRNA expression level.

Gene expression normalization of adjuvant chemotherapy cohort

To compare gene expression data of PD-1 (PDCD1), CD3Z (CD247), CD8A, PD-L1 (CD274), and CXCL9 in the cohort of 102 patients treated with adjuvant platinum-containing chemotherapy, gene expression was normalized by a common approach to calculate Z-Scores [x = sample value (40DCT value in CCC-EMN-cohort; log$_2$-transformed value in the TCGA-cohort); μ = median gene expression in entire cohort; σ = SD of the cohort].

$$Z - \text{Score} = \frac{(x - \mu)}{\sigma}$$

Reference cohort for patients out of the CCC-EMN-Cohort was the entire CCC-EMN-Cohort ($n = 135$). Reference cohort for patients out of the TCGA-Cohort was the entire TCGA-Cohort ($n = 407$). This cohort consists of 69 patients of the TCGA BLCA cohort and 33 patients of the CCC-EMN cohort. Clinicopathologic data of this cohort are displayed in Supplementary Table S1.

TCGA BLCA: Gene expression and mutational data analysis

Assignments for mRNA subtypes, APOBEC mutational load, mutational signatures (MSig), mutational burden [total single-nucleotide variant (SNV) count], and amount of predicted neoantigens were adapted without changes from Robertson and colleagues (3). Tertile assignments of mutational burden and neoantigen load were kindly provided by Jaegil Kim (Broad Institute, Boston, MA) and Gordon Robertson (BC Cancer Agency, Vancouver, Canada). RSEM RNA-seq data were accessed via cBioportal (http://www.cbioportal.org/) and log$_2$-transformed (27).

TCGA BLCA: IC population using the CIBERSORT algorithm

The relative fraction of 22 IC populations based on the whole-exome TCGA RNA-seq dataset was calculated using the CIBERSORT algorithm (https://cibersort.stanford.edu/) with 1,000 permutations (28).

TCGA BLCA: Antigen-presenting cell signature

Cell surface expression of genes in plasmacytoid dendritic cells (pDC), conventional dendritic cells (cDC), and M1 and

M2 macrophages, as well as genes related to antigen processing and presentation, were extracted from the open access pathway analysis database (https://pathcards.genecards.org/) provided by the Weizmann Institute (Rehovot, Israel; Supplementary Table S3).

TCGA BLCA: IC inflammation gene signature

Genes for the IC inflammation signature defining immune cell clusters (ICC) were obtained by coexpression analyses performed with cBioPortal (http://www.cbioportal.org/; ref. 27). The cutoff for gene expression of *CD3Z* and *CD8A* was set at 0.5 SDs from the mean cohort expression (Z-score; see section below for calculations). Genes of interest ($n = 59$) with coexpression correlation (Spearman) of higher than 0.70 were selected (Supplementary Table S4). The gene list ($n = 59$) is also represented in Supplementary Table S4.

Cutoffs and cut-off calculations

The p-quantiles $p = \frac{1}{3}$ and $p = \frac{2}{3}$ were calculated with JMP SAS 13.2 (SAS Institute; tertile split; $T1 < p = \frac{1}{3}$; $p = \frac{1}{3} < T2 < p = \frac{2}{3}$; $T3 > p = \frac{2}{3}$) to split the respective cohorts into three homogenous parts. Tertile ranges in respective subgroups are depicted in Supplementary Table S5.

Statistical analysis

Descriptive statistics were employed to characterize the distributions of continuous variables (mean, SD, SEM, quartiles, median, range) and nominal variables (frequency, percentage). Disease-specific (DSS) and overall survival (OS) curves were estimated by the Kaplan–Meier method. Median potential follow-up was calculated by Reverse Kaplan–Meier analysis. For each subgroup, the number of patients at risk at various milestone time points are shown in a table below the survival plot. Statistical comparisons of subgroups included nonparametric Wilcoxon rank-sum test and Kruskal–Wallis test for continuous variables, Pearson χ^2 test for nominal variables, and log-rank test for time-to-event outcomes. Although a number of related statistical tests were conducted (such as TCGA/all, TCGA/basal, TCGA/luminal), significance adjustment for multiple testing was not performed. Multivariable survival analyses were conducted using Cox proportional hazards regression modeling to assess the magnitude of impact (i.e., the HR) of immune phenotype or sTILs, while adjusting for well-established prognostic clinicopathologic variables [e.g., pT-Stage, pN-Stage, lymphovascular invasion (L), age, gender, presence of distant metastasis, and tumor grading (WHO2016 and WHO1973)]. Variables for final multivariable models were selected by step-wise back and forward selection that is depicted in detail in Supplementary Table S6 for each applied model. Indicator variables were employed to model multilevel nominal variables. All P values were two-sided, and a P value <0.05 was considered statistically significant. Cluster analysis was performed by unsupervised hierarchical clustering based on average link algorithm (WPGMA, weighted pair-group method using arithmetic averages) using Euclidean distance as the metric scale. All statistical analyses were performed by GraphPad Prism 7.2 (GraphPad Software Inc.) and JMP SAS 13.2 (SAS). R 3.3.3 (https://www.r-project.org/) was employed to obtain tertile splits of total single nucleotide variants and predicted neoantigens in the TCGA cohort as described previously (3).

Ethical aspects

This study was approved by the ethical review board of the Friedrich-Alexander-University Erlangen-Nürnberg (Erlangen, Germany; approval number: no. 3755 and 329_16B) in accordance with the Declaration of Helsinki. All patients gave a written informed consent.

Results

High sTILs associate with increased immune cells and checkpoint gene expression

Tumors within the CCC-EMN cohort with high infiltration of sTILs were characterized by dense infiltrates of CD3+, CD8+, CD68+, CD56+, PD-1+, PD-L1+ ICs and high numbers of TLSs (Fig. 1A–C; Supplementary Fig. S1A–S1C). This was in contrast to normal healthy bladder tissue, where significantly lower amounts of sTILs were noted (Supplementary Fig. S1A). We found no association between sTILs and different tumor stages. To test whether sTIL phenotypes render information about the spatial organization of the TIME at the invasive front and tumor center, we performed a hierarchical cluster analysis (Fig. 1A). Four immune tumor phenotypes emerged: (i) cluster A (uninflamed; 36% of cases)—very low infiltration of sTILs (median sTILs: 3%), PD-1+ and PD-L1+ ICs, and absent PD-L1+ TCs (both median: 0%); (ii) cluster B (inflamed-low; 29% of cases)—low sTILs (median sTILs: 10%), including low PD-1+ and PD-L1+ ICs (median: 0.5%) and absence of PD-L1+ TCs (median: 0%); (iii) cluster C (inflamed-high; 22% of cases)—high sTILs (median sTILs: 35%), high PD-1+ and high PD-L1+ IC expression (median: 10%), moderate PD-L1+ TCs (median: 0%; upper quartile 27.5%); and (iv) cluster D (evasion; 13% of cases)—moderate sTILs (median sTILs: 15%), moderate PD-1+ and low PD-L1+ ICs (median: 1.5%) and high PD-L1+ TCs (median: 80%). A disease-specific 5-year survival of patients with inflamed-high tumors (cluster C) was 80.0% (95% CI: 59.6%–91.6%), whereas less than 24.1% (95% CI: 13.8%–38.6%) of patients with uninflamed tumors (cluster A) survived a 5-year period (Fig. 1D). Patients with the evasive tumor phenotype (cluster D) with very high PD-L1 TC expression (4.4-fold compared with cluster C) showed an unfavorable 5-year DSS of 29.3% (95% CI: 11.9%–55.9%; Fig. 1D). Amount of sTILs correlated strongly with different immune cell populations at the invasion front and the tumor center (Fig. 1E).

Gene expression of T-cell genes [*CD3Z* (*CD247*), *CD8A*], a T-cell chemoattractant induced by IFNγ (*CXCL9*), and two immune checkpoints [*PD-1* (*PDCD1*) and *PD-L1* (*CD274*)] associated with high infiltration of sTILs (Fig. 2A and B). Clustering these five genes revealed three hierarchical clusters corresponding with declining amounts of sTILs (median sTILs 40% vs. 3% in the cluster "no" expression; Fig. 2A and B). Tumors with an evasion phenotype assembled throughout all three immune gene clusters (Fig. 2A).

We then quantified TLSs in the peri- and intratumoral stroma, which mediate T cells to the tumor and promote interactions with antigen-presenting cells to generate an antitumoral immune response (refs. 29, 30; Supplementary Fig. S2A and S2B). Tumors with an inflamed-high phenotype had the highest number of TLSs (median: 11 TLSs), whereas the uninflamed and evasion phenotypes had the lowest [uninflamed median: 0 TLS; evasion median: 3 TLS (Fig. 1C)]. The inflamed phenotype correlated with close distances (μm) of TLSs to the tumor-invasive front (median: 37

μm vs. median: 423 μm in uninflamed tumors; Fig. 1C). Close-range localization of TLSs to the tumor (≤129.5 μm; median split), as well as high overall number of TLSs (≥4 TLS; median-split) associated with a significantly higher DSS and emerged as an independent predictor for better DSS in multivariable Cox regression analysis (Supplementary Fig. S2C and S2D; Supplementary Table S6).

High infiltration with sTILs identifies patients with favorable prognosis

Because sTILs can fight tumors, we predicted that sTILs positively influence bladder cancer patient survival. To test this, we applied tertile splitting of the cohort into three equal parts (Supplementary Table S5). Tertile splits revealed that patients with high infiltration of sTILs and high T-cell–associated gene expression have a significantly better DSS (Fig. 2C and D). High sTIL infiltration also was an independent predictor for better DSS in a multivariable Cox regression model (multivariable $P < 0.0001$ for sTILs indicator; Fig. 2C; Supplementary Table S6).

sTIL infiltration is dependent on bladder cancer subtypes

MIBCs can be classified into molecular subtypes (3, 4, 23): luminal, basal, and neuronal/neuroendocrine-like. Depending upon gene expression signatures, several lineage subclasses were also noted by different groups: p53-/EMT-like luminal tumors (MDACC subtyping; ref. 23) and less aggressive luminal papillary tumors, as well as the epithelial mesenchymal transition (EMT)-enriched luminal and luminal-infiltrated tumors [TCGA (3)]. To investigate whether sTILs were associated with tumor subtypes, we performed gene expression subtyping of the CCC-EMN cohort using MDACC subtyping (Supplementary Fig. S3A; ref. 23). Forty-five tumors were assigned as luminal EMT-like/p53-like, 28 as luminal, 52 as basal, and 10 as double negative, whereas 8 showed partial neuroendocrine differentiation (Supplementary Fig. S3A; ref. 23). Basal tumors exhibited the highest sTIL infiltration (Supplementary Fig. S3A). To validate this, we performed unsupervised hierarchical clustering with the same 21 target genes in 407 tumors [TCGA BLCA cohort (Supplementary Fig. S3B)]. A total of 114 tumors were classified as luminal EMT/p53-like, 147 as luminal, 126 as basal, and 20 were double negative (Supplementary Fig. S3B). Congruent with our findings from the CCC-EMN cohort, basal tumors demonstrated the highest sTIL infiltration (Supplementary Fig. S3A and S3B). A correlation of sTILs with tumor subtypes of the TCGA cohort also confirmed that basal squamous tumors exhibited the highest sTILs compared with luminal-infiltrated tumors (second highest count), and luminal and luminal papillary tumors (TCGA subtyping; Fig. 3A).

## Prognostic impact of sTILs in the TCGA cohort

To investigate the prognostic impact of sTILs, we applied tertile-splitting. The tertile split was an independent predictor for better OS in multivariable Cox regression analysis (multivariable $P = 0.0002$ for sTILs indicator; Fig. 3B; Supplementary Table S6). Congruent with a high sTIL infiltration, gene expression of the specific immune cell genes *CD8A*, *CD3Z*, *CXCL9*, and *FOXP3* and immune cell checkpoint–regulatory genes *PDCD1* (*PD-1*), *CD274* (*PD-L1*), *LAG3*, *CTLA4*, and *IDO1* was significantly higher in groups with high sTILs (Fig. 3C).

## The TIME of MIBC correlates with the prognostic impact of sTILs

We predicted that the presence of significantly higher sTILs would correlate with increased antitumor immune responses. Distinct IC populations within the TCGA cohort were calculated (28). Nonparametric Spearman rank correlation revealed correlations of sTILs with the relative amount of all IC populations ($\rho = 0.63$): CD8^{+} T cells ($\rho = 0.49$), NK cells ($\rho = 0.52$), CD4^{+} T cells ($\rho = 0.58$), as well as M1 macrophages ($\rho = 0.63$) and M2 macrophages ($\rho = 0.43$; Fig. 3D; Supplementary Table S3). Unsupervised hierarchical cluster analysis of 59 inflammatory immune cell–related genes in the TCGA cohort was performed to determine correlation of sTILs and IC inflammatory genes (Supplementary Table S4). Three distinct hierarchical inflammation immune cell clusters (ICC) were detected: high inflammation (ICC-high), low inflammation (ICC-low), and uninflamed (Fig. 3A). Inflamed tumors demonstrated high sTIL infiltration and correlated with the basal squamous phenotype (70.3% of ICC-high tumors) and a portion of luminal tumors (ICC-high for 1.0% luminal, 5.9% luminal papillary, and 22.8% luminal-infiltrated; Fig. 3A). A total of 65.9% of luminal papillary tumors were assigned as uninflamed, with lower or no sTILs (Fig. 3A).

We then separately analyzed basal ($n = 142$) and luminal tumors ($n = 243$; Supplementary Table S1) of the TCGA cohort for the same 59 immune genes and sTILs to investigate their importance in the specific subgroups. Three inflammation clusters significantly correlated with sTILs in basal tumors (Fig. 4A; Supplementary Fig. S4A and S4B). Basal MIBC has been reported as the most aggressive subtype, with poor OS (3, 23). However, we found that patients with basal tumors and high infiltration of sTILs have a favorable prognosis (multivariable $P < 0.0001$ for sTILs indicator; Fig. 4B), which is consistent with the inflamed basal-type breast cancer (13). Three inflammation clusters correlating with sTILs were also present in luminal tumors (Fig. 5A; Supplementary Fig. S5A–S5C). Luminal-infiltrated tumors within the ICC-high cluster demonstrated high sTIL infiltration, whereas luminal papillary tumors segregated into the ICC-low and uninflamed gene expression clusters (60% in ICC-low, 85% in uninflamed; Fig. 5A). Although luminal and luminal-infiltrated tumors are considered aggressive with poor prognosis (3), we demonstrated that high infiltration of sTILs were an independent predictor for better OS in these respective subgroups (multivariable $P = 0.027$ for sTILs indicator; Fig. 5B; Supplementary Table S6).

To understand the basis for increased sTILs in the TIME, we tested whether increased somatic tumor mutations could lead to presentation of novel peptides (neoantigens) recognized by the immune system and antitumor activity (8, 31). Tumors with high nonsynonymous single nucleotide variants/high TMB (SNV), a high *APOBEC*-driven mutational burden, and high neoantigen load are indicators for prolonged survival (32). Although these early molecular events have been described for MIBC (3), a direct correlation of these factors with downstream immunologic cells, like sTILs, has not been determined. We found significantly elevated SNVs, *APOBEC*-mediated mutations, and neoantigens in inflamed tumors within the TCGA cohort (Fig. 6A–D; Supplementary Fig. S6). Increased expression of genes mediating antigen presentation, like HLA, also associated with high sTILs and the basal subtype (Supplementary Fig. S7A; Supplementary Table S7). The infiltration of sTILs was significantly higher in subpopulations with high TMB, high neoantigen load, high *APOBEC*-mediated mutational burden,
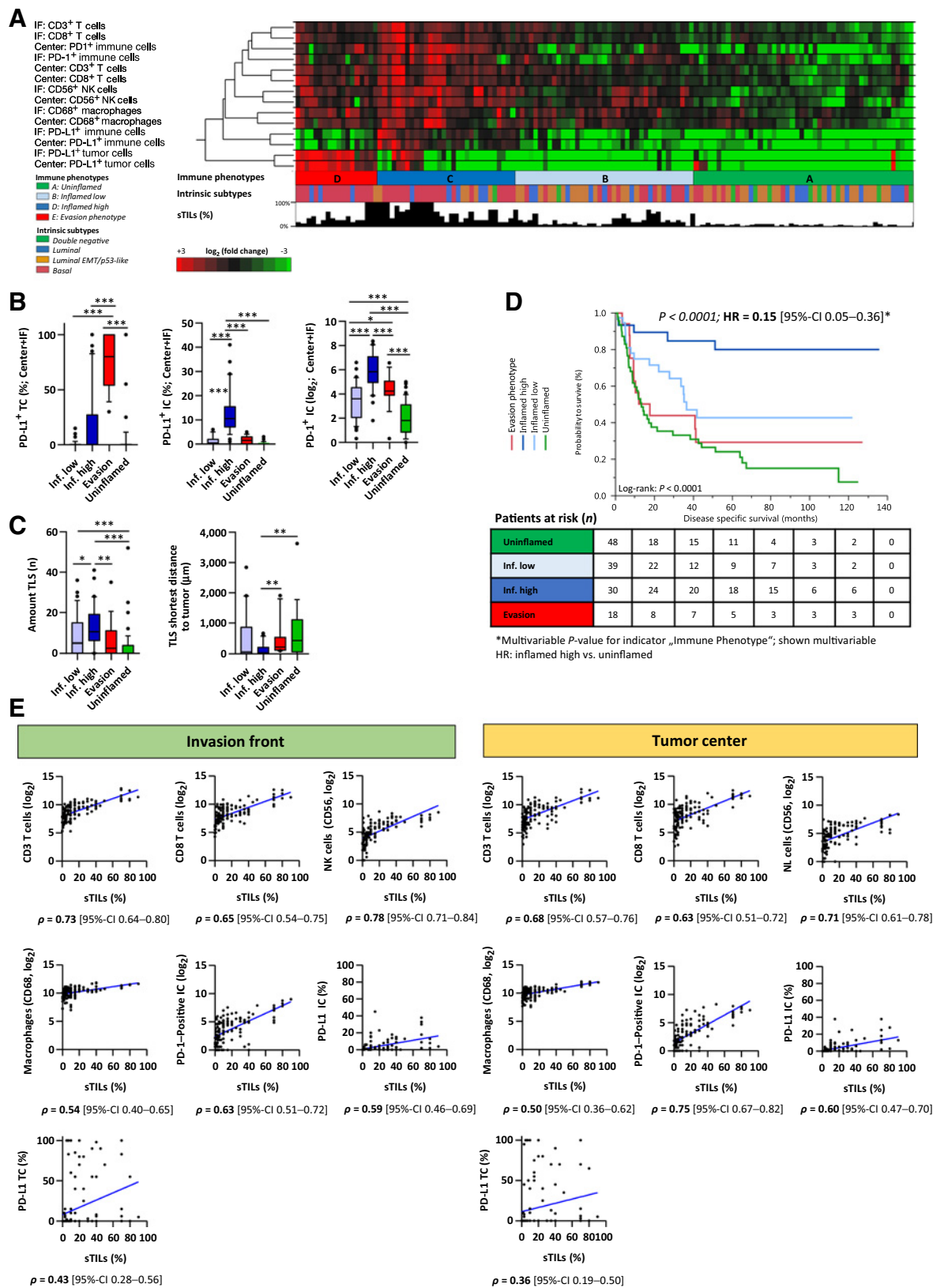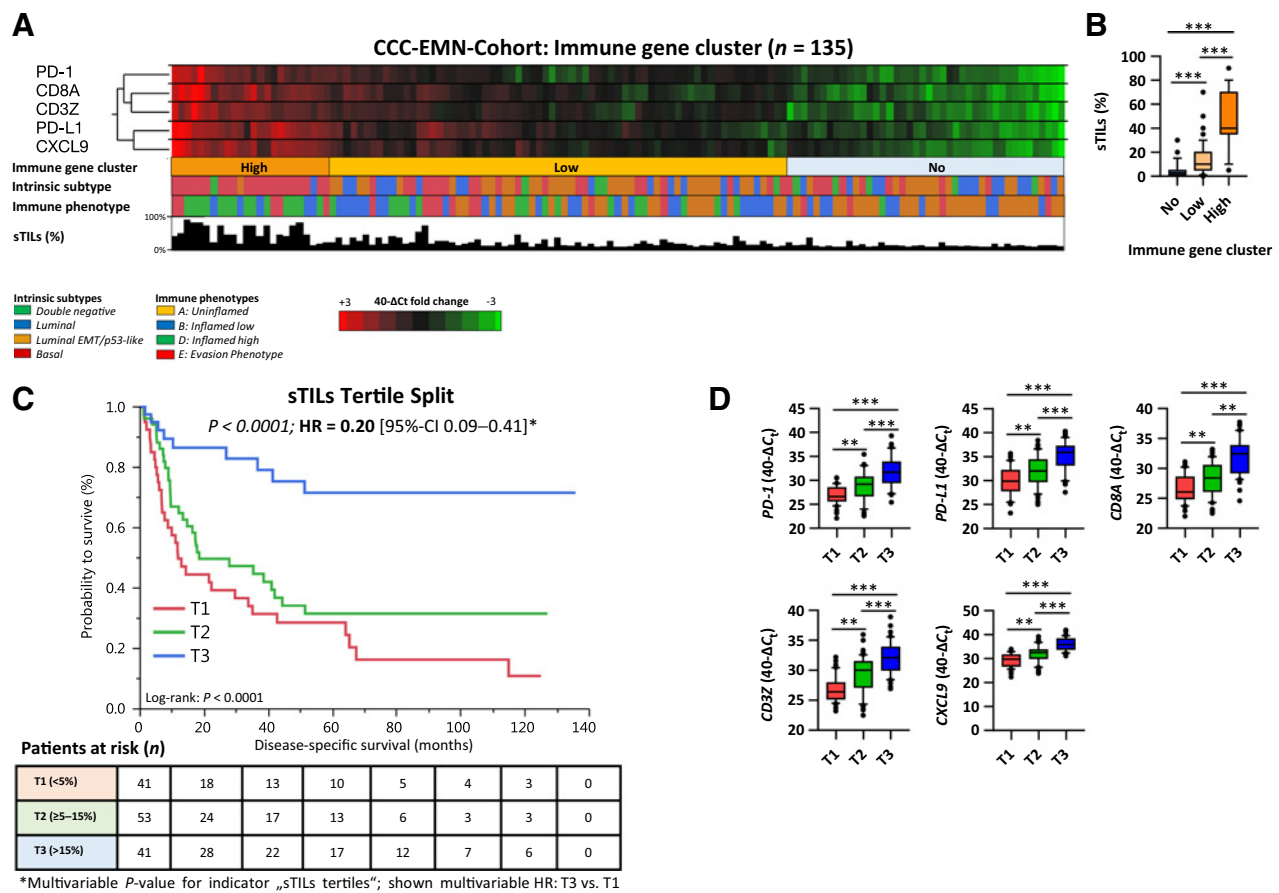
Figure 2.
sTILs and immune gene expression in the CCC-EMN Cohort ($n = 135$). **A,** Immune cell gene expression using unsupervised hierarchical cluster analyses based on the subtypes and phenotypes discussed in Fig. 1A. **B,** Immune gene clusters' infiltration of sTILs. **C,** Kaplan–Meier regression of DSS based on sTILs tertile split (tertile 1–3: T1–T3). Log-rank $P < 0.0001$; multivariable $P < 0.0001$ for indicator "sTILs tertiles." Univariable log-rank P value is depicted in the lower left corner of the survival plot. P value for the entire indicator "sTILs tertiles" derived by multivariable Cox regression is depicted above the survival curves followed by the multivariable HR for Tertile group 3 versus Tertile group 1. The table below the survival plot shows patients at risk in different tertile split groups (first column total amount of patients in each split group) with following columns showing the number of patients at risk in 20-month increments. **D,** Immune gene expression (PDCD1, CD274, CXCL9, CD3A, CD3Z) based on tertile groups (*, $P < 0.05$; **, $P < 0.01$; ***, $P < 0.001$ tested by Mann–Whitney test).

and distinct mutational signatures described by Robertson and colleagues (MSig; ref. 3; Fig. 6B).

sTILs correlate with better survival after adjuvant platinum-containing chemotherapy

High sTIL infiltration is an indicator for a favorable outcome after peri-operative chemotherapy in breast cancer (13). Plati-num-based chemotherapeutic agents enhance antitumor immu-nomodulatory mechanisms, such as recruitment and stimulating proliferation of T_{EFF} cells (33). To investigate whether patients treated with cis- or carbo-platinum adjuvant chemotherapy showed a dependency on sTIL levels and profited from therapy, we combined 69 patients from the TCGA and 33 patients from the CCC-EMN cohorts (Supplementary Table S1 and S5;
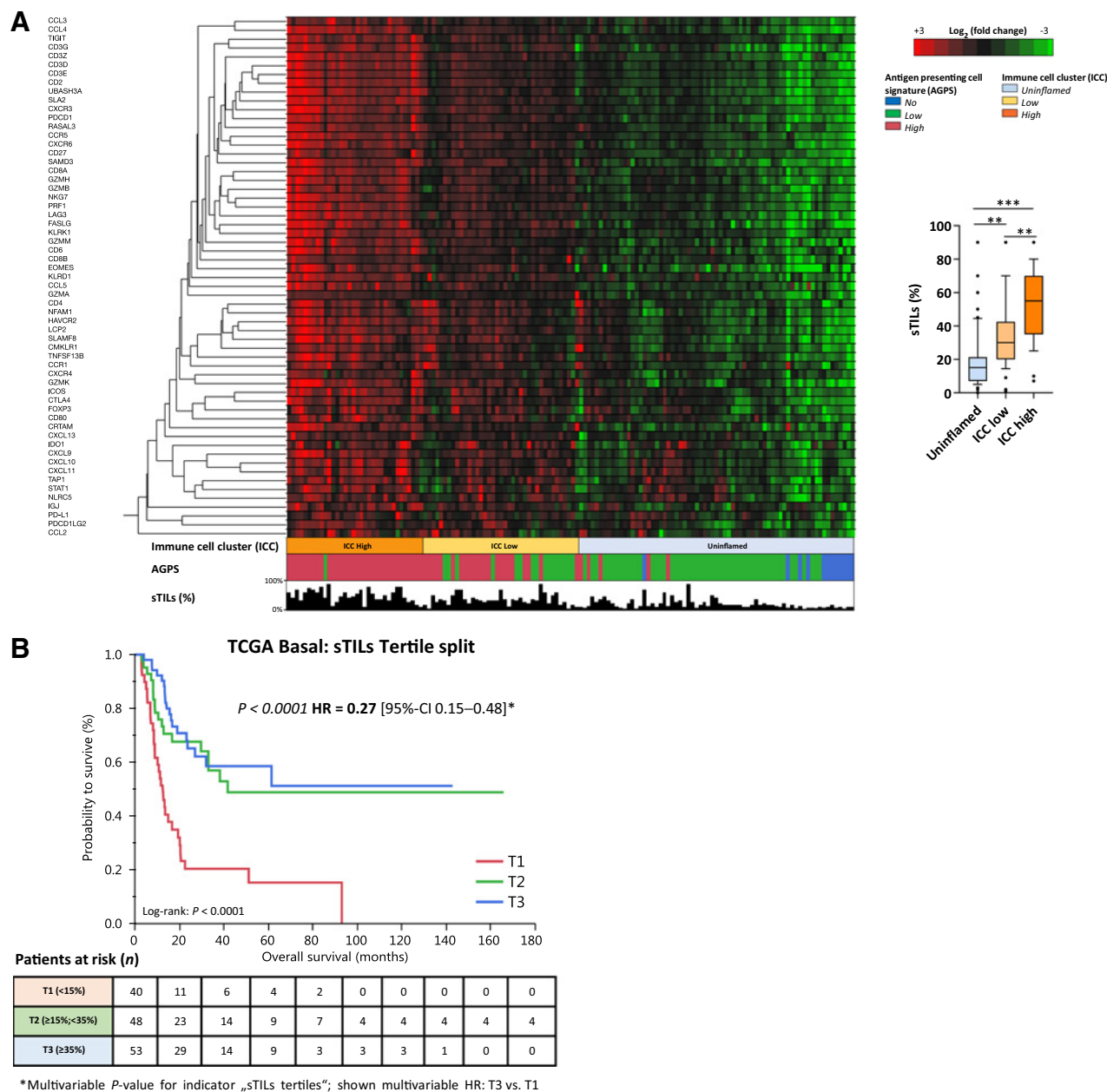
Figure 1.
Hierarchical clustering of tumor immune cell phenotypes of the CCC-EMN cohort. **A,** sTILs and macrophages according to immune cell phenotypes (left) and spatial tumor location (IF, invasion front; center, tumor center; TC, tumor cells; IC, immune cells). Unsupervised hierarchical cluster analyses (average-linkage algorithm) representing the absolute cell counts per mm^2 (log$_2$-transformed) revealed four tumor immune phenotypes (indicated on the left and below the heatmap). Four clusters were revealed: Cluster A (uninflamed), cluster B (inflamed-low), cluster C (inflamed-high), and cluster D (evasion. sTILs in percent (shown below heatmap, scale in percent, left). **B,** Percentage of PD-L1$^+$ TCs (left) and ICs (middle), as well as count of PD-1$^+$ ICs (right) according to immune phenotypes described in **A**. **C,** Number and distances (µm) of tertiary lymphoid structure (TLS)-containing lymphocytes and their association with tumor phenotypes shown in **A** (*, $P < 0.05$; **, $P < 0.01$; ***, $P < 0.001$; tested by Mann–Whitney test). **D,** Kaplan–Meier regression of disease-specific survival (DSS) based on immune cell phenotypes. Univariable log-rank P value is depicted in the lower left corner of the survival plot. P value for the entire indicator "immune phenotypes" derived by multivariable Cox regression is depicted above the survival curves, followed by the multivariable HR for inflamed-high versus uninflamed. Table shows total patients/phenotype with the following columns showing the number of patients at risk in 20-month increments. **E,** Nonparametric Spearman rank correlations (Spearman ρ) of sTILs scores with counts of CD3$^+$ and CD8$^+$ T cells, CD68$^+$ macrophages, PD-1$^+$ immune cells, CD56$^+$ NK cells, and PD-L1 scoring of ICs and TCs.
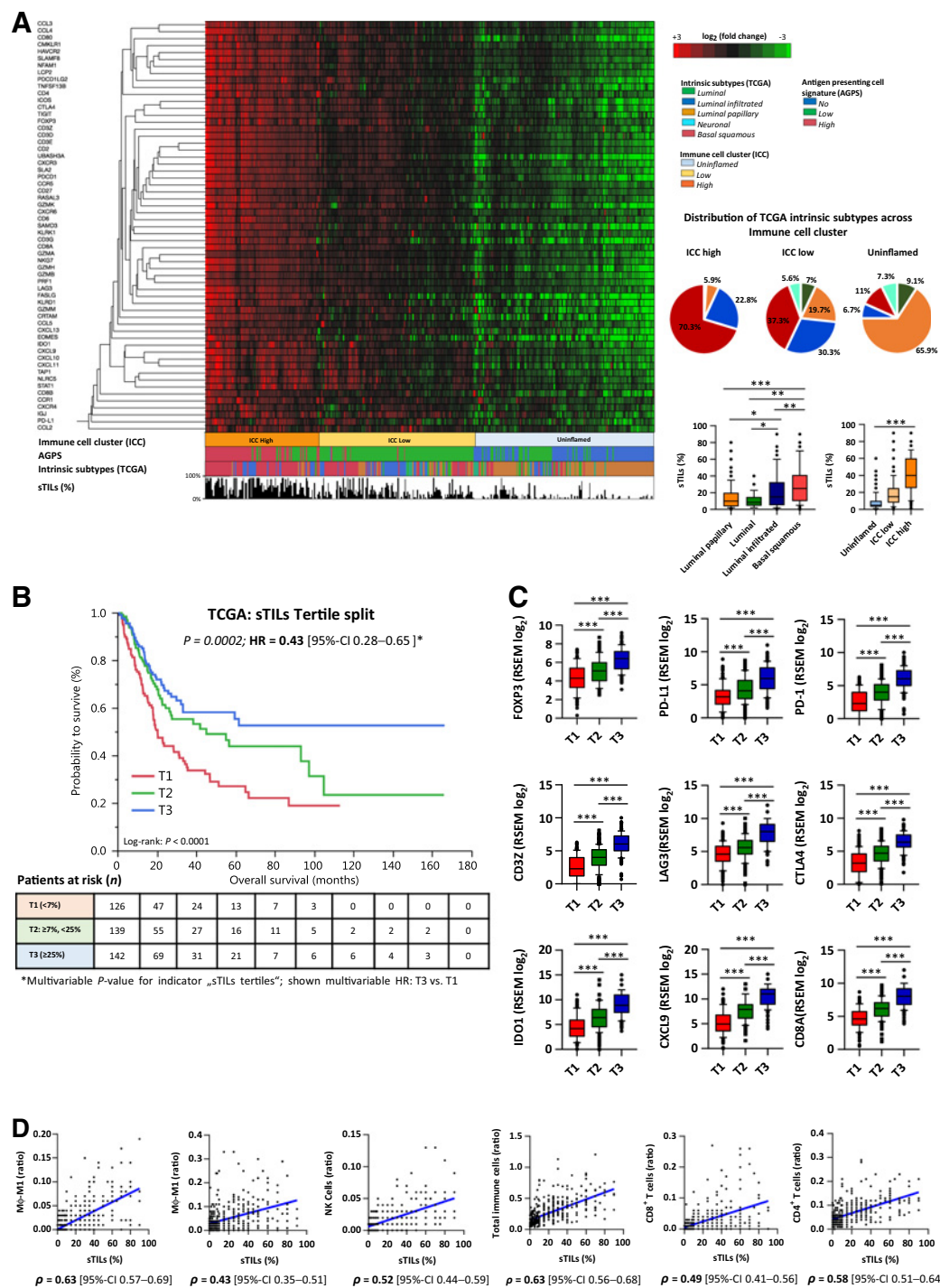
Figure 3.

TCGA-TIME ($n = 407$). **A,** Unsupervised hierarchical clustering of 59 genes related to immune cell inflammation revealed three immune cell clusters (ICC): Inflamed-high, inflamed-low, and uninflamed. Distribution of tumor subtypes and correlation with the antigen-presenting cell signature (AGPS) are indicated below ICC clusters, as well as in pie distributions (right) and graphs with sTILs (%) (right). **B,** Kaplan–Meier regression of survival based on sTILs tertile split (T1–T3). Log-rank $P < 0.0001$; multivariable $P = 0.0002$ for indicator "sTILs tertiles." Univariable log-rank P value is depicted in the lower left corner of the survival plot. P value for the entire indicator "sTILs tertiles" derived by multivariable Cox regression is depicted above the survival curves followed by the multivariable HR for "Tertile group 3" versus "Tertile group 1". Table shows tertile split groups (first column total number of patients) with following columns showing the number of patients at risk in 20-month increments. **C,** Cytotoxic T_{EFF} and Th cells (*CXCL9, CD3A, CD3Z*) and immune checkpoint [*CTLA4, IDO1, PDCD-1 (PD-1), CD274 (PD-L1), LAG3*] gene expression based on tertile split (*, $P < 0.05$; **, $P < 0.01$; ***, $P < 0.001$; tested by Mann–Whitney test). **D,** Spearman rank correlations (Spearman ρ) of sTILs and different immune cell populations calculated by CIBERSORT algorithm.
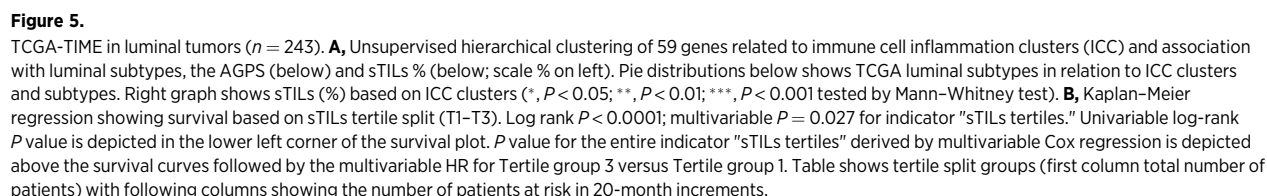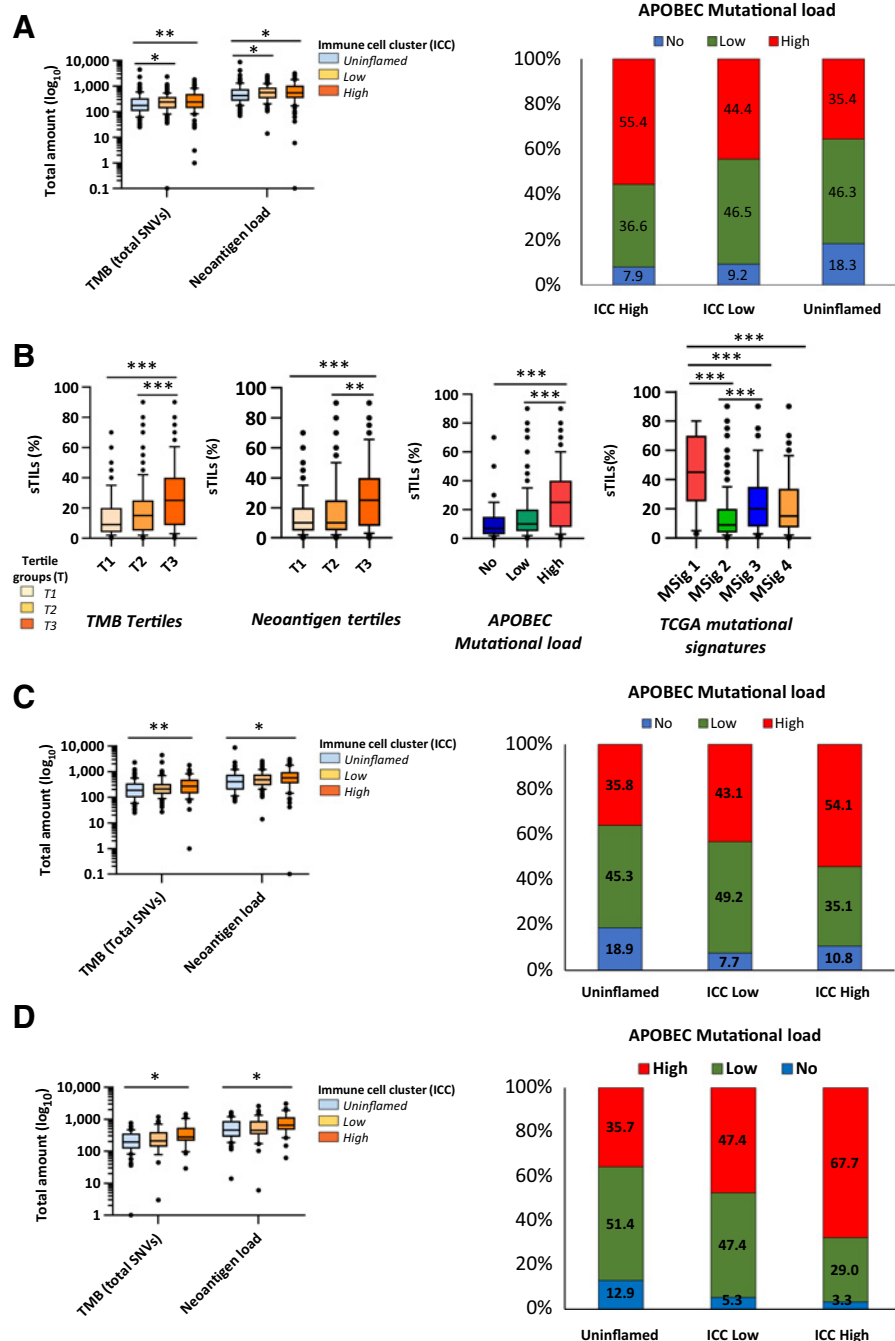
Figure 4.
TCGA-TIME in basal tumors ($n = 142$). **A,** Unsupervised hierarchical clustering of 59 genes related to immune cell inflammation clusters (ICC) and association with the AGPS (below) and sTILs (%; below; scale in % on left) in basal differentiated tumors. Right graph shows sTILs (%) based on ICC clusters (*, $P < 0.05$; **, $P < 0.01$; ***, $P < 0.001$) tested by Mann–Whitney test. **B,** Kaplan–Meier regression showing survival based on sTILs tertile split (T1–T3). Log-rank $P < 0.0001$; multivariable $P = 0.0002$ for indicator "sTILs tertiles". Univariable log-rank P value is depicted in the lower left corner of the survival plot. P value for the entire indicator "sTILs tertiles" derived by multivariable Cox regression is depicted above the survival curves followed by the multivariable HR for Tertile group 3 versus Tertile group 1. Table shows Tertile split groups (first column total number of patients) with following columns showing the number of patients at risk in 20-month increments.

Supplementary Fig. S7B). Unsupervised hierarchical clustering of *PDCD1*, *CD274*, *CD3Z*, *CD8A*, and *CXCL9* defined three immune gene expression clusters. The high cluster was represented by 61.9% basal tumors and 38.1% luminal tumors with the highest sTILs (median sTILs count: 27% vs. 7% for low sTILs and 5% for no sTILs; Fig. 7A and B; Supplementary Fig. S7A).

Tertile splitting revealed that high sTILs associated with increased patient overall survival after chemotherapy [multivariable $P = 0.0001$ for sTILs indicator; multivariable HR = 0.22 (Tertile group 3 vs. Tertile group 1); Fig. 7C; Supplementary Table S6] and increased immune cell inflammation–related gene expression (Fig. 7D). A total of 65.1% of
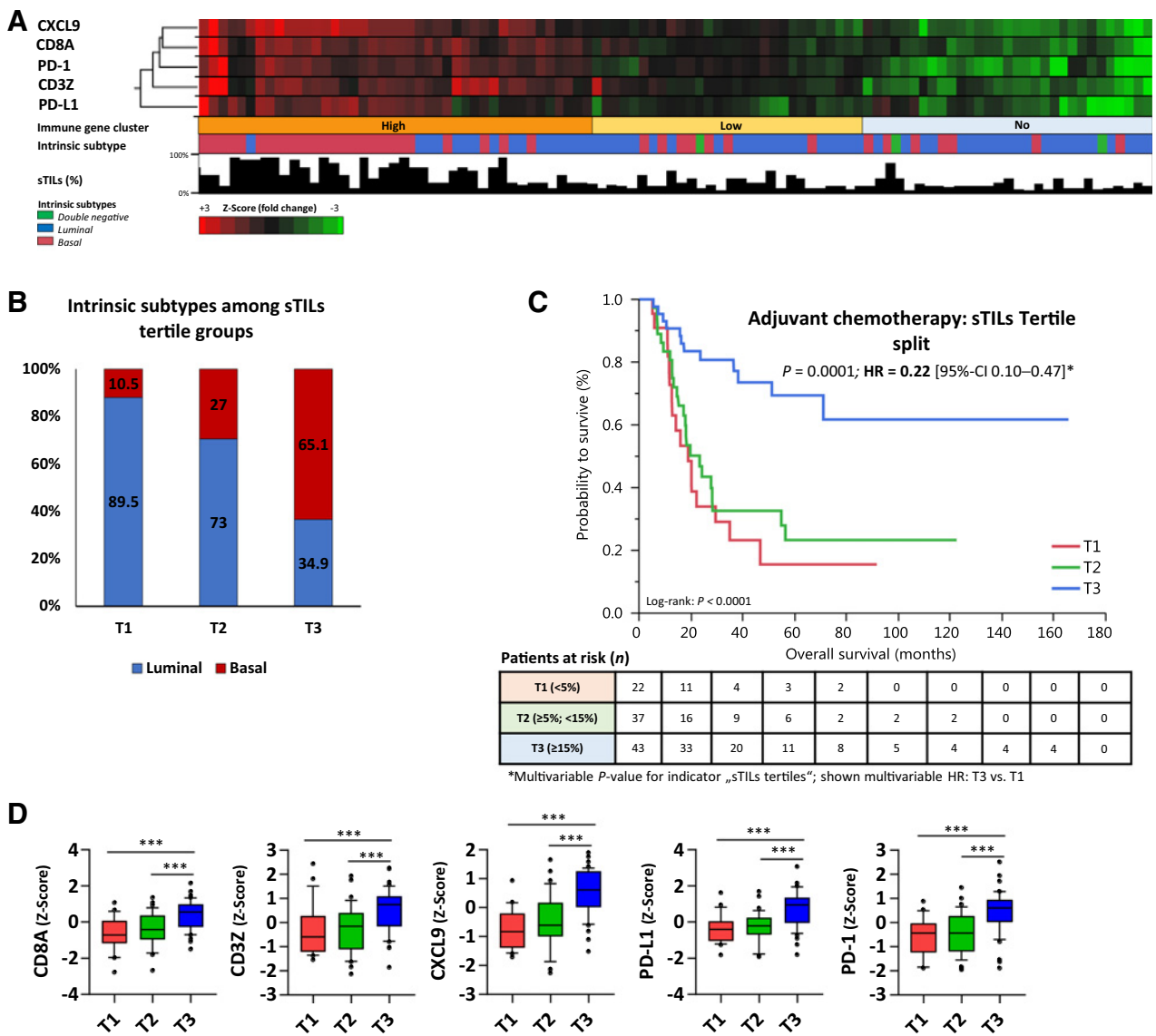
Figure 5.

TCGA-TIME in luminal tumors (n = 243). **A,** Unsupervised hierarchical clustering of 59 genes related to immune cell inflammation clusters (ICC) and association with luminal subtypes, the AGPS (below) and sTILs % (below; scale % on left). Pie distributions below shows TCGA luminal subtypes in relation to ICC clusters and subtypes. Right graph shows sTILs (%) based on ICC clusters (*, P < 0.05; **, P < 0.01; ***, P < 0.001 tested by Mann–Whitney test). **B,** Kaplan–Meier regression showing survival based on sTILs tertile split (T1–T3). Log rank P < 0.0001; multivariable P = 0.027 for indicator "sTILs tertiles." Univariable log-rank P value is depicted in the lower left corner of the survival plot. P value for the entire indicator "sTILs tertiles" derived by multivariable Cox regression is depicted above the survival curves followed by the multivariable HR for Tertile group 3 versus Tertile group 1. Table shows tertile split groups (first column total number of patients) with following columns showing the number of patients at risk in 20-month increments.

Figure 6.
Correlation of SNVs, neoantigens, *APOBEC* mutational load, and mutational signatures in TCGA. **A,** Total SNVs (SNVs/TMB; $\log_{10}$) and neoantigen load ($\log_{10}$), as well as the *APOBEC* mutation load based on different ICC clusters within the entire TCGA cohort. **B,** Percentage of sTILs in the entire TCGA cohort based on tertile groups and TMB, neoantigen load, *APOBEC*-mediated mutational burden, and distinct mutational signatures (MSig). ICC gene clusters' total SNVs/TMB, neoantigen load, and *APOBEC* mutational burden in basal (**C**) and luminal subtypes (**D**) (*P* value abbreviations *, $P < 0.05$; **, $P < 0.01$; ***, $P < 0.001$ tested by Mann–Whitney test).

the tumors within Tertile group 3 were basal. These results indicated that patients with basal and luminal tumors, with high sTILs, benefit from adjuvant platinum-containing chemotherapy. This is in line with reports demonstrating a favorable outcome of patients with breast cancer treated with neoadjuvant chemotherapy for basal-like tumors with high sTILs (13, 34), and for neoadjuvant chemotherapy of patients with basal MIBC, which show increased chemoresponsiveness (4). In line with these observations, a nonsignificant trend for better survival ($P = 0.055$) was found for patients with basal-differentiated MIBC undergoing adjuvant chemotherapy (Supplementary Fig. S7C).

Discussion

Following tumor antigen presentation in lymph nodes, TILs including T, B, and NK cells are primed to mount a powerful immunologic inflammatory response to tumor cells. Negative T-cell checkpoint inhibitors engage with ligands, like PD-1 with PD-L1, to ensure a balanced immune response to avoid an autoimmune reaction (35). Unfortunately, within the TIME the resulting inflammatory immune response is not sufficient to eradicate all tumor cells and is subject to regulation, including immunosuppression and inflammatory cytokines which fuel tumor progression (36).

Figure 7.
Prognostic impact of sTILs in patients treated with adjuvant chemotherapy (*n* = 102). **A,** Unsupervised hierarchical clustering of five immune cell inflammation genes with a combined cohort of 69 patients with TCGA MIBC and 33 patients with MIBC from the CCC-EMN (*n* = 102), treated with adjuvant chemotherapy (platinum-based). Immune cell gene clusters are shown below (high, low, no), stromal TILs (%; scale %, left) and the tumor subtypes. **B,** Percentage of luminal and basal subtypes according to sTILs tertile split (T1–T3). **C,** Kaplan–Meier regression of survival of patients with MIBC (*n* = 102) treated with adjuvant chemotherapy (platinum-based) based on sTILs tertile split (T1–T3). Log-rank *P* < 0.0001; multivariable *P* = 0.0001 for indicator "sTILs tertiles". Univariable log-rank *P* value is depicted in the lower left corner of the survival plot. *P* value for the entire indicator "sTILs tertiles" derived by multivariable Cox regression is depicted above the survival curves, followed by the multivariable HR for Tertile group 3 versus Tertile group 1. Table shows tertile split groups (first column total number of patients) with following columns showing the number of patients at risk in 20-month increments. **D,** Gene expression based on sTILs tertile split (T1–T3; *, *P* < 0.05; **, *P* < 0.01; ***, *P* < 0.001 tested by Mann–Whitney test).

The main impact of this study was the identification of a role of sTILs in the TIME, whose specific quantities and spatial organization phenotypes predicted antitumor inflammation that associated with patient survival, as well as with molecular tumor subtypes. Using sTILs and a panel of five key T-cell–specific and inflammation genes, we could delineate high, low, or absent tumor inflammation, which was like a 59 immune cell gene cluster within the TCGA cohort. High

tumor inflammation was significantly enriched in basal tumors, whereas low inflammation mainly associated with luminal subtypes. High sTILs and inflammation predicted improved patient survival. High TMB, *APOBEC* mutation, and neoantigen load in MIBC correspond with a favorable 5-year OS of 75% (3). We showed that a high *APOBEC* signature mutational load, high TMB, and neoantigen load could be responsible for an increased expression of recognizable antigens with

consecutive upregulation of antigen-presenting–related genes, such as MHC-I and MHC-II class HLA genes, leading to high sTILs infiltration and antitumor inflammation, and could explain improved patient outcome.

IHC and gene expression analysis of the CCC-EMN-cohort revealed immune cell phenotypes, which were spatially organized and correlated with numbers of sTILs and amounts, distance, and localization of TLSs. We identified two inflamed phenotypes with favorable outcomes and an uninflamed phenotype, as well as a tumor evasion phenotype with high PD-L1 TC expression, with the latter two both associated with adverse outcomes.

An important factor within the TIME are TLSs, which in addition to lymph nodes, can also exhibit antitumor activity via antigen presentation, leading to an efflux of active immune cells (29, 30). Here, high amounts and close tumor distance of TLSs correlated significantly with a favorable DSS. Both the uninflamed and evasion phenotypes showed the lowest amount and the farthest TLS distances, resulting in the shortest DSS. These findings support a negative regulation of immune cells occurring in the TIME. The inflamed-high phenotype, as well as tumors enriched with TLSs, also exhibited high *CXCL9*. This was validated in the TCGA cohort, including other chemokines of the CXC and CC cytokine subfamilies, which play a positive role in antitumor activity in the TIME.

The importance of investigating sTILs and the spatial arrangement of the TIME stemmed from patients with bladder cancer treated with platinum-based chemotherapy or checkpoint inhibitors. High amounts of sTILs in patients with metastatic UBC treated with a platinum-based chemotherapy indicate prolonged OS (37). Patients with metastatic UBC with high neoantigens and TMB, as well as enrichment of $CD8^+$ T_{EFF} cells, show higher objective response rates toward atezolizumab (5). In liver metastasis, sTILs and PD-L1 expression are significantly reduced compared with matched primary tumors (38), and patients respond worse to checkpoint inhibition (6).

Studies have demonstrated the relevance of UBC tumor subtypes for response to checkpoint inhibition (6). In both cohorts (CCC-EMN/TCGA), uninflamed immune phenotypes were prominently enriched for luminal subtypes, whereas inflamed-high subtypes were mainly basal tumors. Luminal tumors enriched with an EMT-like gene expression signature associated with low to moderate inflammation and immune checkpoint expression. These tumors are aggressive tumors (3), characterized by low proliferation with chemoresistance (3, 23). EMT-enriched luminal tumors have been shown to evade immunosurveillance by upregulation of the TGFβ axis (5). Other immune evasion mechanisms could lead to sTILs exclusion: (i) tumor recruitment of suppressive myeloid cells, such as myeloid-derived suppressor cells (MDSC), tumor-associated macrophages (TAM), immature DCs, and immunosuppressive neutrophils, leading to poor tumor migration and invasion of $CD8^+$ T cells (39, 40); (ii) establishment of a glucose-poor tumor microenvironment by tumor cells, limiting metabolism of TILs (41); (iii) intratumoral delivery of cytokines, chemokines, and upregulation of other immune checkpoints by tumor cells to restrict T-cell function (42); and (iv) deregulation of chemokine expression by tumor endothelial cells, preventing T-cell homing (42).

The incapacitated immune response observed in uninflamed tumors in our study cohorts, mainly luminal tumors, may be a factor for poor responsiveness to checkpoint inhibition and lower survival of first-line–treated patients with low or absent PD-L1 expression (43). These patients should not solely be candidates for anti–PD-L1 or anti–PD-1 immune checkpoint inhibitor therapy, but need alternative strategies to possibly initiate an immune response. Preclinical work from several groups has shown the potential of therapies that modulate the cancer epigenome to reverse immune evasion in the TIME. DNA methyltransferase inhibitors (DNMTi) remove suppressive DNA methylation marks and activate endogenous retro-elements that can be sensed by the innate immune system, resulting in an antiviral response (44–46). This antiviral IFN response recruits and activates host immune cells to the TIME (47) and sensitizes melanoma (44), lung (47), and ovarian (47) mouse cancer models to immune checkpoint blockade therapy. Most favorable tumor responses were seen when DNMTis were combined with another epigenetic therapy, like histone deacetylase inhibitors (47). Separately, DNMTis can also reverse T_{EFF} cell exhaustion, reinvigorating them to fight tumors and sensitizing them to immune checkpoint blockade (48). Clinical trials are currently under way in several solid tumors testing the efficacy of this combination of epigenetic and immune therapy (NCT02816021, NCT03019003, NCT01928576, NCT02959437).

Tumors with inflamed-high and evasion phenotypes were mainly represented by basal tumors, which harbor important implications for their treatment. For example, inflamed-high tumors with moderate to high PD-1 and PD-L1 expression, exclusively on immune cells, seem to represent an immune phenotype with a normal restriction on active T_{EFF} cells. A fraction of these tumors also showed increased PD-L1 expression on tumor cells. Because both phenotypes demonstrated a favorable prognosis with the highest DSS, this supports antitumor activity by sTILs. The immune evasion phenotype showed a worse prognosis, which could be due to having the highest constitutive PD-L1 tumor expression, which can lead to sTIL exhaustion (49). We conclude all the tumor phenotypes above would be suitable for PD-L1 or PD-1–targeting therapies to further unleash an antitumor immune response in inflamed-high tumors and recapacitate the antitumor immune responses in tumors with evasion phenotype.

All of the above findings, except the specific immune phenotypes by IHC, were confirmed in the TCGA cohort. Classical luminal tumors are characterized by low proliferation, and we now showed that they also have low amounts of sTILs, low to absent expression of immune checkpoint markers, and a low TMB. This indicated that neither chemotherapy nor immune therapy are suitable for those tumors but support a potential benefit from other therapies, like epigenetic modulators, to ignite an immune response that could be enhanced by an immune checkpoint blockade (3, 6). The observed tumor subtype dependency of immune infiltrates in MIBC is similar to breast cancer (13, 50). Among the different immune phenotypes revealed in this study, we propose that assessment of sTILs is a prognostic factor that allows risk stratification after radical cystectomy. We demonstrated an independent survival advantage of high sTILs and immune cell phenotypes by analyzing all MIBCs, as well as specific subgroups, separately stratified by tumor differentiation or therapy. The prognostic value of sTIL assessment is independent of basal and EMT-like phenotypes. Thus, this assessment adds information for risk stratification of patients with aggressive tumor phenotypes

(luminal EMT-like, basal tumors). These associations are in line with findings in breast cancer (13). High amount of sTILs predicted a benefit of adjuvant platinum-containing chemotherapy. The most benefited subpopulation had enriched basal differentiation, which has also been shown to be a favorable predictive factor for responsiveness to neoadjuvant chemotherapy (4). Platinum-containing chemotherapy has been shown to increase DCs, eliminate MDSCs (51), enhance NK-cell–mediated antitumor toxicity (52), and increase $CD8^+$ T_{EFF}-cell–mediated antitumor responses (53). Although cystectomy removes the majority of tumor cells, this positive effect could be explained by enhanced antitumor immune responses, with increased local and circulating tumor cell clearance (54). Further support for the above shows that chemotherapeutic agents can induce proliferation of memory $CD4^+$ and $CD8^+$ T cells that are critical for sustained antitumor immunity (55). Beside the enhancement effects of platinum-containing chemotherapy, our findings support the idea that memory T and B cells play a critical role in sustained antitumor activity after complete tumor resection. Memory immune cells could perform tumor cell clearance of circulating tumor cells or metastatic tumor cells at distal sites, which would result in long-term protective immunity to prevent relapse and improve patient survival. Studies regarding resident memory $CD8^+$ T cells in patients with breast cancer demonstrate a correlation with improved survival (56, 57).

Our current investigation supports a rationale that sTILs, TLSs, and immune cell phenotypes, along with tumor subtypes of MIBC, are factors for risk stratification. On the basis of our findings, patients with the uninflamed and low-inflamed tumor phenotypes with unfavorable prognosis (64 % of MIBC) would need alternative therapies to (re)ignite the immune system. Patients with inflamed-high tumors or with an evasion phenotype could benefit from immune checkpoint blockade. Our findings could potentially improve MIBC patient treatment design to personalized therapy for a better outcome.

Limitations are the use of OS data to calculate survival of the TCGA cohort and the merged adjuvant chemotherapy (only OS available). In TCGA survival analyses, age was the most adverse risk factor for poor OS, which is most likely the cause for frequent, nontumor-specific causes of death in these patients. However, all multivariable analyses in this study were adjusted for age and other available demographic characteristics in Cox proportional hazard analyses. In the CCC-EMN cohort, limited numbers of survival events in respective analytic subgroups may have contributed to precision and power issues. Thus, upcoming studies with larger case numbers are needed to further validate the prognostic impact of immune phenotypes.

Disclosure of Potential Conflicts of Interest

Authors' Contributions

Conception and design: P.L. Strissel, R. Wirtz, M. Burger, B. Wullich, C. Bolenz, P. Erben, A. Hartmann, R. Strick, M. Eckstein
Development of methodology: R. Wirtz, A. Hartmann, M. Eckstein
Acquisition of data (provided animals, acquired and managed patients, provided facilities, etc.): C. Pfannstiel, D. Sikic, R. Wirtz, A. Wullweber, H. Taubert, W. Otto, M. Burger, C. Bolenz, N. Fuhrich, C.I. Geppert, R. Stoehr, S. Bertz, B. Keck, A. Hartmann, M. Eckstein
Analysis and interpretation of data (e.g., statistical analysis, biostatistics, computational analysis): C. Pfannstiel, P.L. Strissel, K.B. Chiappinelli, R. Wirtz, H. Taubert, M. Burger, N. Fuhrich, V. Weyerer, S. Bertz, F. Erlmeier, R. Strick, M. Eckstein
Writing, review, and/or revision of the manuscript: C. Pfannstiel, P.L. Strissel, K.B. Chiappinelli, D. Sikic, S. Wach, A. Wullweber, H. Taubert, J. Breyer, W. Otto, T. Worst, M. Burger, B. Wullich, C. Bolenz, C.I. Geppert, V. Weyerer, R. Stoehr, S. Bertz, B. Keck, F. Erlmeier, P. Erben, A. Hartmann, R. Strick, M. Eckstein
Administrative, technical, or material support (i.e., reporting or organizing data, constructing databases): C. Pfannstiel, S. Wach, A. Wullweber, W. Otto, B. Wullich, C. Bolenz, C.I. Geppert, R. Stoehr, M. Eckstein
Study supervision: P.L. Strissel, W. Otto, C. Bolenz, A. Hartmann, R. Strick, M. Eckstein

Acknowledgments

References

1. Antoni S, Ferlay J, Soerjomataram I, Znaor A, Jemal A, Bray F. Bladder cancer incidence and mortality: a global overview and recent trends. Eur Urol 2017;71:96–108.
2. Alfred Witjes J, Lebret T, Comperat EM, Cowan NC, De Santis M, Bruins HM, et al. Updated 2016 EAU guidelines on muscle-invasive and metastatic bladder cancer. Eur Urol 2017;71:462–75.
3. Robertson AG, Kim J, Al-Ahmadie H, Bellmunt J, Guo G, Cherniack AD, et al. Comprehensive molecular characterization of muscle-invasive bladder cancer. Cell 2018;174:1033.
4. Seiler R, Ashab HA, Erho N, van Rhijn BW, Winters B, Douglas J, et al. Impact of molecular subtypes in muscle-invasive bladder cancer on predicting response and survival after neoadjuvant chemotherapy. Eur Urol 2017;72:544–54.
5. Mariathasan S, Turley SJ, Nickles D, Castiglioni A, Yuen K, Wang Y, et al. TGFbeta attenuates tumour response to PD-L1 blockade by contributing to exclusion of T cells. Nature 2018;554:544–8.
6. Bellmunt J, Powles T, Vogelzang NJ. A review on the evolution of PD-1/PD-L1 immunotherapy for bladder cancer: The future is now. Cancer Treat Rev 2017;54:58–67.
7. Topalian SL, Drake CG, Pardoll DM. Immune checkpoint blockade: a common denominator approach to cancer therapy. Cancer Cell 2015; 27:450–61.

8. Schumacher TN, Schreiber RD. Neoantigens in cancer immunotherapy. Science 2015;348:69–74.

9. Dieu-Nosjean MC, Antoine M, Danel C, Heudes D, Wislez M, Poulot V, et al. Long-term survival for patients with non-small-cell lung cancer with intratumoral lymphoid structures. J Clin Oncol 2008;26:4410–7.

10. Catalona WJ, Mann R, Nime F, Potvin C, Harty JI, Gomolka D, et al. Identification of complement-receptor lymphocytes (B cells) in lymph nodes and tumor infiltrates. J Urol 1975;114:915–21.

11. Zitvogel L, Apetoh L, Ghiringhelli F, Andre F, Tesniere A, Kroemer G. The anticancer immune response: indispensable for therapeutic success? J Clin Invest 2008;118:1991–2001.

12. Pages F, Mlecnik B, Marliot F, Bindea G, Ou FS, Bifulco C, et al. International validation of the consensus Immunoscore for the classification of colon cancer: a prognostic and accuracy study. Lancet 2018;391:2128–39.

13. Denkert C, von Minckwitz G, Darb-Esfahani S, Lederer B, Heppner BI, Weber KE, et al. Tumour-infiltrating lymphocytes and prognosis in different subtypes of breast cancer: a pooled analysis of 3771 patients treated with neoadjuvant therapy. Lancet Oncol 2018;19:40–50.

14. Goode EL, Block MS, Kalli KR, Vierkant RA, Chen W, Fogarty ZC, et al. Dose-response association of CD8+ tumor-infiltrating lymphocytes and survival time in high-grade serous ovarian cancer. JAMA Oncol 2017;3: e173290.

15. Zhang L, Conejo-Garcia JR, Katsaros D, Gimotty PA, Massobrio M, Regnani G, et al. Intratumoral T cells, recurrence, and survival in epithelial ovarian cancer. N Engl J Med 2003;348:203–13.

16. Sweis RF, Spranger S, Bao R, Paner GP, Stadler WM, Steinberg G, et al. Molecular drivers of the non-T-cell-inflamed tumor microenvironment in urothelial bladder cancer. Cancer Immunol Res 2016;4:563–8.

17. Ren R, Tyryshkin K, Graham CH, Koti M, Siemens DR. Comprehensive immune transcriptomic analysis in bladder cancer reveals subtype specific immune gene expression patterns of prognostic relevance. Oncotarget 2017;8:70982–1001.

18. Sharma P, Shen Y, Wen S, Yamada S, Jungbluth AA, Gnjatic S, et al. CD8 tumor-infiltrating lymphocytes are predictive of survival in muscle-invasive urothelial carcinoma. Proc Natl Acad Sci U S A 2007;104: 3967–72.

19. Sjodahl G, Lovgren K, Lauss M, Chebil G, Patschan O, Gudjonsson S, et al. Infiltration of CD3(+) and CD68(+) cells in bladder cancer is subtype specific and affects the outcome of patients with muscle-invasive tumors. Urol Oncol 2014;32:791–7.

20. Hendry S, Salgado R, Gevaert T, Russell PA, John T, Thapa B, et al. Assessing tumor-infiltrating lymphocytes in solid tumors: a practical review for pathologists and proposal for a standardized method from the International Immuno-Oncology Biomarkers Working Group: Part 2: TILs in melanoma, gastrointestinal tract carcinomas, non-small cell lung carcinoma and mesothelioma, endometrial and ovarian carcinomas, squamous cell carcinoma of the head and neck, genitourinary carcinomas, and primary brain tumors. Adv Anat Pathol 2017;24:311–35.

21. Eckstein M, Wirtz RM, Pfannstil C, Wach S, Stoehr R, Breyer J, et al. A multicenter round robin test of PD-L1 expression assessment in urothelial bladder cancer by immunohistochemistry and RT-qPCR with emphasis on prognosis prediction after radical cystectomy. Oncotarget 2018;9: 15001–14.

22. Eckstein M, Erben P, Kriegmair MC, Worst TS, Weiss CA, Wirtz RM, et al. Performance of the Food and Drug Administration/EMA-approved programmed cell death ligand-1 assays in urothelial carcinoma with emphasis on therapy stratification for first-line use of atezolizumab and pembrolizumab. Eur J Cancer 2019;106:234–43.

23. Choi W, Porten S, Kim S, Willis D, Plimack ER, Hoffman-Censits J, et al. Identification of distinct basal and luminal subtypes of muscle-invasive bladder cancer with different sensitivities to frontline chemotherapy. Cancer Cell 2014;25:152–65.

24. Breyer J, Otto W, Wirtz RM, Wullich B, Keck B, Erben P, et al. ERBB2 expression as potential risk-stratification for early cystectomy in patients with pT1 bladder cancer and concomitant carcinoma in situ. Urol Int 2017; 98:282–9.

25. Breyer J, Wirtz RM, Otto W, Erben P, Worst TS, Stoehr R, et al. High PDL1 mRNA expression predicts better survival of stage pT1 non-muscle-invasive bladder cancer (NMIBC) patients. Cancer Immunol Immunother 2018;67: 403–12.

26. Bustin SA, Benes V, Garson JA, Hellemans J, Huggett J, Kubista M, et al. The MIQE guidelines: minimum information for publication of quantitative real-time PCR experiments. Clin Chem 2009;55:611–22.

27. Cerami E, Gao J, Dogrusoz U, Gross BE, Sumer SO, Aksoy BA, et al. The cBio cancer genomics portal: an open platform for exploring multidimensional cancer genomics data. Cancer Discov 2012;2:401–4.

28. Newman AM, Liu CL, Green MR, Gentles AJ, Feng W, Xu Y, et al. Robust enumeration of cell subsets from tissue expression profiles. Nat Methods 2015;12:453–7.

29. Joshi NS, Akama-Garren EH, Lu Y, Lee DY, Chang GP, Li A, et al. Regulatory T cells in tumor-associated tertiary lymphoid structures suppress anti-tumor T cell responses. Immunity 2015;43:579–90.

30. Buisseret L, Desmedt C, Garaud S, Fornili M, Wang X, Van den Eyden G, et al. Reliability of tumor-infiltrating lymphocyte and tertiary lymphoid structure assessment in human breast cancer. Mod Pathol 2017;30: 1204–12.

31. Giannakis M, Mu XJ, Shukla SA, Qian ZR, Cohen O, Nishihara R, et al. Genomic correlates of immune-cell infiltrates in colorectal carcinoma. Cell Rep 2016;15:857–65.

32. Middlebrooks CD, Banday AR, Matsuda K, Udquim KI, Onabajo OO, Paquin A, et al. Association of germline variants in the APOBEC3 region with cancer risk and enrichment with APOBEC-signature mutations in tumors. Nat Genet 2016;48:1330–8.

33. de Biasi AR, Villena-Vargas J, Adusumilli PS. Cisplatin-induced antitumor immunomodulation: a review of preclinical and clinical evidence. Clin Cancer Res 2014;20:5384–91.

34. Gu-Trantien C, Loi S, Garaud S, Equeter C, Libin M, de Wind A, et al. CD4 (+) follicular helper T cell infiltration predicts breast cancer survival. J Clin Invest 2013;123:2873–92.

35. Thommen DS, Schumacher TN. T Cell Dysfunction in Cancer. Cancer Cell 2018;33:547–62.

36. Maman S, Witz IP. A history of exploring cancer in context. Nat Rev Cancer 2018;18:359–76.

37. Huang HS, Su HY, Li PH, Chiang PH, Huang CH, Chen CH, et al. Prognostic impact of tumor infiltrating lymphocytes on patients with metastatic urothelial carcinoma receiving platinum based chemotherapy. Sci Rep 2018;8:7485.

38. Eckstein M, Sikic D, Strissel PL, Erlmeier F, Germany BC. Evolution of PD-1 and PD-L1 gene and protein expression in primary tumors and corresponding liver metastases of metastatic bladder cancer. Eur Urol 2018;74:527–9.

39. Gabrilovich DI, Ostrand-Rosenberg S, Bronte V. Coordinated regulation of myeloid cells by tumours. Nat Rev Immunol 2012;12:253–68.

40. Peranzoni E, Lemoine J, Vimeux L, Feuillet V, Barrin S, Kantari-Mimoun C, et al. Macrophages impede CD8 T cells from reaching tumor cells and limit the efficacy of anti-PD-1 treatment. Proc Natl Acad Sci U S A 2018;115: E4041–50.

41. Ho PC, Bihuniak JD, Macintyre AN, Staron M, Liu X, Amezquita R, et al. Phosphoenolpyruvate is a metabolic checkpoint of anti-tumor T cell responses. Cell 2015;162:1217–28.

42. Joyce JA, Fearon DT. T cell exclusion, immune privilege, and the tumor microenvironment. Science 2015;348:74–80.

43. Gourd E. EMA restricts use of anti-PD-1 drugs for bladder cancer. Lancet Oncol 2018;19:e341.

44. Chiappinelli KB, Strissel PL, Desrichard A, Li H, Henke C, Akman B, et al. Inhibiting DNA methylation causes an interferon response in cancer via dsRNA including endogenous retroviruses. Cell 2015;162: 974–86.

45. Roulois D, Loo Yau H, Singhania R, Wang Y, Danesh A, Shen SY, et al. DNA-demethylating agents target colorectal cancer cells by inducing viral mimicry by endogenous transcripts. Cell 2015;162:961–73.

46. Licht JD. DNA methylation inhibitors in cancer therapy: the immunity dimension. Cell 2015;162:938–9.

47. Topper MJ, Vaz M, Chiappinelli KB, DeStefano Shields CE, Niknafs N, Yen RC, et al. Epigenetic therapy ties MYC depletion to reversing immune evasion and treating lung cancer. Cell 2017; 171:1284–300.

48. Ghoneim HE, Fan Y, Moustaki A, Abdelsamed HA, Dash P, Dogra P, et al. De novo epigenetic programs inhibit PD-1 blockade-mediated T cell rejuvenation. Cell 2017;170:142–57.

49. Ribas A, Hu-Lieskovan S. What does PD-L1 positive or negative mean? J Exp Med 2016;213:2835–40.

50. Wang K, Xu J, Zhang T, Xue D. Tumor-infiltrating lymphocytes in breast cancer predict the response to chemotherapy and survival outcome: a meta-analysis. Oncotarget 2016;7:44288–98.

51. Chen J, Huang X, Huang G, Chen Y, Chen L, Song H. Preconditioning chemotherapy with cisplatin enhances the antitumor activity of cytokine-induced killer cells in a murine melanoma model. Cancer Biother Radiopharm 2012;27:210–20.

52. Gasser S, Orsulic S, Brown EJ, Raulet DH. The DNA damage pathway regulates innate immune system ligands of the NKG2D receptor. Nature 2005;436:1186–90.

53. Vincent J, Mignot G, Chalmin F, Ladoire S, Bruchard M, Chevriaux A, et al. 5-Fluorouracil selectively kills tumor-associated myeloid-derived suppressor cells resulting in enhanced T cell-dependent antitumor immunity. Cancer Res 2010;70:3052–61.

54. Bracci L, Schiavoni G, Sistigu A, Belardelli F. Immune-based mechanisms of cytotoxic chemotherapy: implications for the design of novel and rationale-based combined treatments against cancer. Cell Death Differ 2014;21: 15–25.

55. Schiavoni G, Mattei F, Di Pucchio T, Santini SM, Bracci L, Belardelli F, et al. Cyclophosphamide induces type I interferon and augments the number of CD44(hi) T lymphocytes in mice: implications for strategies of chemoimmunotherapy of cancer. Blood 2000;95:2024–30.

56. Natarajan P, Liu D, Patel SR, Santhanakrishnan M, Beitler D, Liu J, et al. CD4 depletion or CD40L blockade results in antigen-specific tolerance in a red blood cell alloimmunization model. Front Immunol 2017;8:907.

57. Enamorado M, Iborra S, Priego E, Cueto FJ, Quintana JA, Martinez-Cano S, et al. Enhanced anti-tumour immunity requires the interplay between resident and circulating memory CD8(+) T cells. Nat Commun 2017;8: 16073.